REVIEW

Pulse EPR Methods for Studying Chemical and Biological Samples Containing Transition Metals

by **Carlos Calle**, **Anandaram Sreekanth**, **Matvey V. Fedin**, **Jörg Forrer**, **Inés Garcia-Rubio**, **Igor A. Gromov**, **Dariush Hinderberger**, **Besnik Kasumaj**, **Patrick Léger**, **Bruno Mancosu**, **George Mitrikas**, **Maria Grazia Santangelo**, **Stefan Stoll**, **Arthur Schweiger**[1]), **René Tschaggelar**, and **Jeffrey Harmer***

Laboratory of Physical Chemistry, Department of Chemistry and Applied Biosciences, ETH Zurich,
8093 Zurich, Switzerland
(e-mail: harmer@phys.chem.ethz.ch)

In memoriam Professor *Hanns Fischer*

This review discusses the application of pulse EPR to the characterization of disordered systems, with an emphasis on samples containing transition metals. Electron nuclear double-resonance (ENDOR), electron-spin-echo envelope-modulation (ESEEM), and double electron–electron resonance (DEER) methodologies are outlined. The theory of field modulation is outlined, and its application is illustrated with DEER experiments. The simulation of powder spectra in EPR is discussed, and strategies for optimization are given. The implementation of this armory of techniques is demonstrated on a rich variety of chemical systems: several porphyrin derivatives that are found in proteins and used as model systems, otherwise highly reactive aminyl radicals stabilized with electron-rich transition metals, and nitroxide–copper–nitroxide clusters. These examples show that multi-frequency continuous-wave (CW) and pulse EPR provides detailed information about disordered systems.

Contents

---

[1]) Deceased on January 4, 2006.

1. Introduction. – Electron-paramagnetic-resonance (EPR) spectroscopy is a powerful method for studying paramagnetic samples, *i.e.*, systems containing one or more unpaired electrons. EPR Spectroscopy can provide unique information on the electronic structure since the magnetic parameters such as *g* values, hyperfine couplings, and nuclear quadrupole interactions are directly related to the electronic wavefunction and the configuration of the surrounding nuclei. The *g* values and, for species with several unpaired electrons ($S > \frac{1}{2}$), the zero-field splittings often provide fingerprint information on the type of paramagnetic species. The hyperfine couplings characterize the spin populations[2] [1] in detail and can be used to measure distances between the nuclei and the unpaired electron up to *ca.* 1 nm. The nuclear quadrupole interactions provide information on the bonding of nuclei and can also be utilized to determine bond angles. For these reasons, EPR spectroscopy is well suited for structural studies in systems lacking long-range order on length scales that are not easily accessible by other techniques.

This review focuses on EPR techniques used to study paramagnetic samples in disordered systems, with an emphasis on transition-metal complexes. In powders, frozen solutions, and even single crystals, many of the hyperfine and nuclear-quadrupole splittings are not resolved in the field-swept EPR spectrum due to inhomogeneous broadening effects. Electron nuclear double-resonance (ENDOR) and electron-spin-echo envelope-modulation (ESEEM) methods provide much higher resolution by directly measuring nuclear frequencies and thus provide information on strong to very weak interactions. This allows the fine details of the system to be studied. To get long-range information (1–8 nm), the distance between two unpaired electrons can be measured by means of double electron–electron resonance (DEER), or an alternative technique presented in this review by using a bichromatic pulse consisting of a microwave (m.w.) and a radio frequency (r.f.) pulse.

The present review is structured as follows. In *Sect. 2*, the most important terms of the spin Hamiltonian and the concept of orientation selection in disordered systems is introduced, and a nuts and bolts description of ENDOR, ESEEM, and the DEER technique is given. In *Sect. 3*, the application of these techniques is then demonstrated on a range of transition-metal complexes with a variety of ligands. The first group comprises porphyrin derivatives which are employed by nature in many proteins and by chemists and materials scientists as catalysts [2]. The complexes described are the Cu^{II} complex of N-confused tetraphenylporphyrin, the Ni-containing cofactor F$_{430}$ in the active site of methylcoenzyme M reductase, and the heme macrocycle, *i.e.*, (porphyrinato)iron. The second group of complexes show how reactive aminyl radicals can be stabilized by coordination to the electron-rich transition-metal rhodium. These complexes are potentially very efficient catalysts as they combine the variable oxidation states of a transition metal with a very reactive radical. The third example shows how to characterize a high-spin system with multi-frequency continuous-wave (CW) EPR, a nitroxide–copper–nitroxide cluster coupled by a strong exchange interaction.

---

[2]   *Spin density* $\rho(x,y,z)$ denotes the difference in the number of electrons per unit volume having spin up and down: $\rho(x,y,z) = \rho^\alpha(x,y,z) - \rho^\beta(x,y,z)$. *Spin population* ρ_x^ψ is interpretable as the integrated spin density $\rho(x,y,z)$ in the orbital ψ centered on nucleus *x* and is the difference in the populations of unpaired electrons with spin up and spin down, $\rho_x^\psi = \rho_x^{\psi\alpha} - \rho_x^{\psi\beta}$.

2. EPR Basics. – Following is a concise description of the theory and techniques discussed in this review. A comprehensive treatment of pulse EPR methodology is given in [3], or the review articles [4–10] provide good introductions.

2.1. *Static Spin Hamiltonian.* The static spin Hamiltonian $\mathscr{H}_0$ describes the energies of states of a paramagnetic species in the ground state with an effective electron spin S and m nuclei with nuclear spins I (*Eqns. 1a* and *1b*).

$$\mathscr{H}_0 = \mathscr{H}_{EZ} + \mathscr{H}_{ZFS} + \mathscr{H}_{HF} + \mathscr{H}_{NZ} + \mathscr{H}_{NQ} \tag{1a}$$

$$= \beta_e \tilde{\mathbf{B}}_0 \mathbf{g} \mathbf{S}/\hbar + \tilde{\mathbf{S}} \mathbf{D} \mathbf{S} + \sum_{k=1}^{m} \tilde{\mathbf{S}} \mathbf{A}_k \mathbf{I}_k - \beta_n \sum_{k=1}^{m} g_{n,k} \tilde{\mathbf{B}}_0 \mathbf{I}_k/\hbar + \sum_{k=1; I_k > 1/2}^{m} \tilde{\mathbf{I}}_k \mathbf{P}_k \mathbf{I}_k \tag{1b}$$

In this review, all interactions are given in angular-frequency units unless stated otherwise. $\mathscr{H}_0$ is called the spin Hamiltonian since it contains only phenomenological constants and spin coordinates described by the electron-spin vector operator $\tilde{\mathbf{S}} = [\hat{S}_x, \hat{S}_y, \hat{S}_z]$ and the nuclear-spin vector operators $\tilde{\mathbf{I}}_k = [\hat{I}_{x,k}, \hat{I}_{y,k}, \hat{I}_{z,k}]$. $\mathbf{B}_0$ is a 3×1 vector describing the direction and strength of the permanent magnetic field. The transpose is denoted with ˜. The terms in *Eqns. 1* have the following meaning: $\mathscr{H}_{EZ}$, electron *Zeeman* interaction; $\mathscr{H}_{ZFS}$, zero-field splitting; $\mathscr{H}_{HF}$, hyperfine interactions between the electron spins and the m nuclear spins; $\mathscr{H}_{NZ}$, nuclear *Zeeman* interactions; and $\mathscr{H}_{NQ}$, nuclear quadrupole interactions for $I > \frac{1}{2}$. The information that one seeks to determine experimentally are the 3×3 matrices $\mathbf{g}$, $\mathbf{D}$, $\mathbf{A}$, and $\mathbf{P}$.

In the case of two electron spins S_1 and S_2 that are weakly coupled, such as in a biradical, it is most convenient to describe the individual spins S_1 and S_2 with an exchange coupling J and dipolar tensor $\mathbf{D}_{dd}$, (*Eqn. 2*).

$$\mathscr{H}_{ss} = -2J \tilde{\mathbf{S}}_1 \mathbf{S}_2 + \tilde{\mathbf{S}}_1 \mathbf{D}_{dd} \mathbf{S}_2 \tag{2}$$

For negative J, the triplet state ($S = 1$) of the two electrons is higher in energy than the singlet ($S = 0$), and the coupling is antiferromagnetic. For positive J, the triplet is stabilized relative to the singlet and the coupling is ferromagnetic. Measurement of the dipole coupling tensor $\mathbf{D}_{dd}$, for example by DEER experiments, allows the electron–electron distance to be calculated according to *Eqn. 3*, where $\mathbf{D}_{dd}$ is in its principal axes frame and g_1 and g_2 are the g values of the two electrons.

$$\mathbf{D}_{dd} = \frac{\mu_0}{4\pi\hbar} \frac{g_1 g_2 \beta_e^2}{r_{12}^3} \begin{pmatrix} -1 & & \\ & -1 & \\ & & 2 \end{pmatrix} = \begin{pmatrix} -\omega_{dd} & & \\ & -\omega_{dd} & \\ & & 2\omega_{dd} \end{pmatrix} \tag{3}$$

2.2. *Orientation Selection in Pulse EPR.* The absorption spectrum of a paramagnetic center in a frozen solution or in a powder is anisotropic, usually the electron *Zeeman* interaction gives the largest contribution. For organic radicals, the anisotropy is small, and it is often possible to excite the entire spectrum with a short intense m.w. pulse (*Fourier*-transform EPR). In transition-metal complexes, the situation is typically

very different, the width of the absorption spectrum (*ca.* 1 GHz) is much larger than the effective excitation bandwidth of the m.w. pulse (*ca.* 50 MHz). This orientationally selective excitation allows the magnetic interactions with respect to the *g*-matrix coordinate system to be estimated. The orientation selection for the orthorhombic spectrum of MCR_{red2} (see *Sect. 3.1.2.*) is shown in *Fig. 1*.

2.3. *Origin of the Nuclear Modulation Effect.* The energy levels of an $S = \frac{1}{2}$, $I = \frac{1}{2}$ spin system are shown in *Fig. 2*. In this four-level system, there are two allowed ($\Delta m_S = \pm 1$, $\Delta m_I = 0$) and two forbidden ($\Delta m_S = \pm 1$ and $\Delta m_I = \pm 1$) EPR transitions. These are excited in a CW-EPR measurement. ENDOR and ESEEM techniques aim to directly measure the nuclear frequencies ω_α and ω_β ($\Delta m_S = 0$, $\Delta m_I = \pm 1$).

The nuclear frequencies ω_α and ω_β of the two spin system are given by *Eqn. 4*, where *A* and *B* describe the secular and pseudo-secular part of the hyperfine coupling. In the case of an axially symmetric hyperfine interaction, *Eqn. 5* holds, where θ is the polar angle between $\mathbf{B}_0$ and the electron-nuclear vector. The transition probabilities of the allowed (I_a) and forbidden (I_f) EPR transitions are given by *Eqn. 6*, where 2η is the angle between the nuclear quantization axes in the two m_S manifolds, ω_I is the *Larmor* frequency, $\omega_+ = \omega_\alpha + \omega_\beta$ and $\omega_- = \omega_\alpha - \omega_\beta$.

$$\omega_\alpha = |\omega_{12}| = \left[\left(\omega_I + \frac{A}{2}\right)^2 + \left(\frac{B}{2}\right)^2\right]^{1/2}, \quad \omega_\beta = |\omega_{34}| = \left[\left(\omega_I - \frac{A}{2}\right)^2 + \left(\frac{B}{2}\right)^2\right]^{1/2} \quad (4)$$

$$A = a_{iso} + T(3\cos^2\theta - 1), \ B = 3T \sin\theta \cos\theta \quad (5)$$

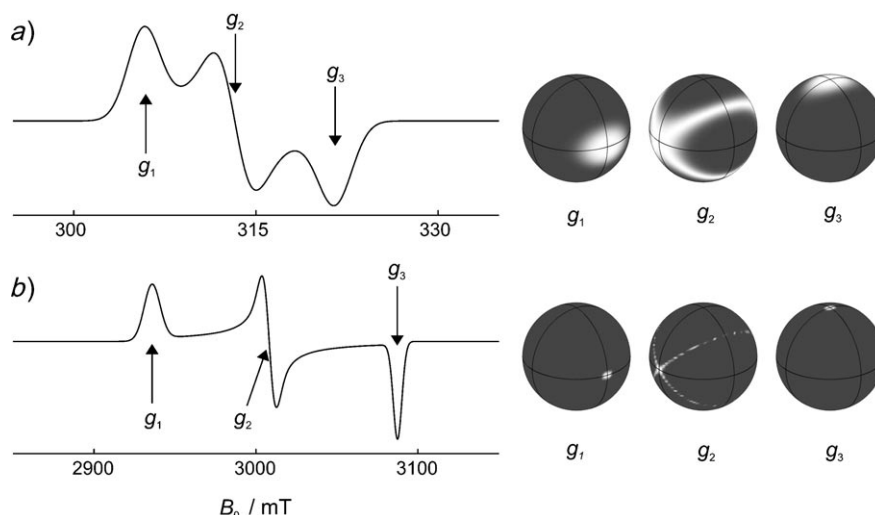Fig. 1. *Calculated EPR spectra* (left) *and orientation selection* (right) *on the unit sphere for the observer* (B_0 field) *positions corresponding to* g_1, g_2, *and* g_3. a) *X-band* (9.8 GHz)*, and* b) *W-band* (94.1 GHz). White indicates orientations on-resonance with the m.w. pulse, black shading is off-resonance. The m.w. pulse for the orientation selection used a bandwidth of 30 MHz. The EPR spectrum is a simulation of the MCR_{red2} species with $g_1 = 2.290$, $g_2 = 2.235$, $g_3 = 2.178$.
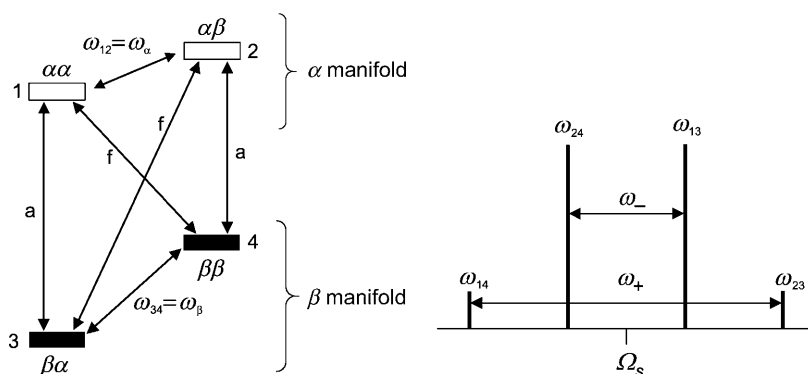
Fig. 2. *Energy-level diagram* (left) *and corresponding schematic EPR spectrum* (right) *for an* $S=\frac{1}{2}$, $I=\frac{1}{2}$ *model system with* $|A_S| < |2\omega_I|$ (weak-coupling case). a: allowed EPR transitions (1,3) and (2,4); f: forbidden EPR transitions (1,4) and (2,3); nuclear transitions (1,2) and (3,4). A_s is the hyperfine coupling at an arbitrary orientation.

$$I_a = \cos^2 \eta = \frac{\left| \omega_I^2 - \frac{1}{4}\omega_-^2 \right|}{\omega_\alpha \omega_\beta}, \quad I_f = \sin^2 \eta = \frac{\left| \omega_I^2 - \frac{1}{4}\omega_+^2 \right|}{\omega_\alpha \omega_\beta} \tag{6}$$

ESEEM Techniques rely on the excitation of both allowed and forbidden EPR transitions using m.w. radiation. For example, the nuclear coherence generator $\pi/2 - \tau - \pi/2$ (see below, *Fig. 3*) is used in three-pulse ESEEM and HYSCORE experiments. There is no ESEEM effect if $I_f = 0$. This excludes the measurement of isotropic hyperfine couplings ($T=0 \rightarrow B=0$) and the principal values of the hyperfine couplings ($\theta=0$, $\pi/2 \rightarrow B=0$). Note that when $B=0$, $\omega_+ = 2\omega_I$. The former precludes the measurement of hyperfine couplings of paramagnetic centers in solution if the observed couplings are averaged to a_{iso} by rapid molecular tumbling.

In ENDOR spectroscopy, nuclear frequency spectra are measured by direct irradiation of the nuclear transitions with r.f. radiation.

2.4. *ESEEM.* The nuclear modulation effect was first observed by *Rowan*, *Hahn*, and *Mims* [11], and the theory was later developed by *Mims* in 1972 [12]. The three most used sequences are given in *Fig. 3*.

In the two-pulse ESEEM experiment (*Fig. 3,a*) the intensity of the primary echo is recorded as a function of the time interval τ between the $\pi/2$ and π pulses. The echo amplitude modulation formula for an $S=\frac{1}{2}$, $I=\frac{1}{2}$ system is given by *Eqn. 7*, where k is the orientation-dependent modulation depth parameter given by *Eqn. 8*. For the case of an isotropic hyperfine interaction[3] $\mathbf{A} = a_{iso}\mathbf{I}$, or if $\mathbf{B}_0$ is oriented along one of the principal axes of the hyperfine tensor ($\theta=0$ or $\theta=\pi/2$), the echo modulation disappears, since B in *Eqn. 8* is zero. The modulation depth is largest when $|A_S| \approx 2|\omega_I|$.

---

[3] Isotropic part of the hyperfine interaction, $a_{iso} = (A_1 + A_2 + A_3)/3$; dipolar part of the hyperfine interaction, $(T_1, T_2, T_3) = (A_1 - a_{iso}, A_2 - a_{iso}, A_3 - a_{iso})$. A_s is the hyperfine coupling at an arbitrary orientation.
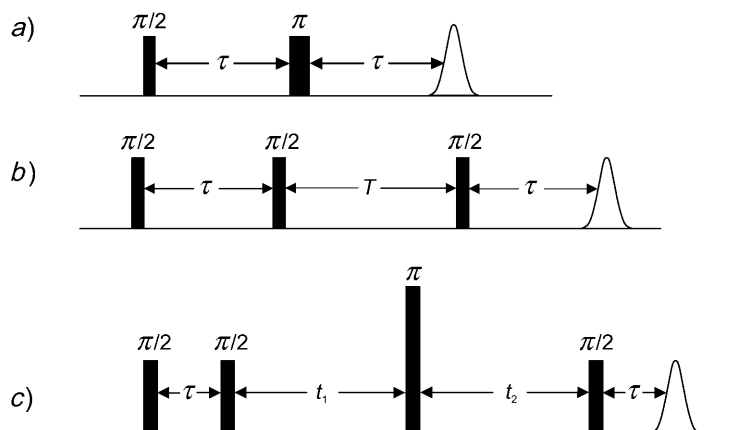
Fig. 3. Pulse sequences making use of the ESEEM effect: a) *Two-pulse sequence and the primary echo,* b) *three-pulse sequence for producing a stimulated echo, and* c) *four-pulse sequence for the HYSCORE experiment*

$$V_{2p}(\tau) = 1 - \frac{k}{4}[2 - 2\cos(\omega_\alpha\tau) - 2\cos(\omega_\beta\tau) + \cos(\omega_-\tau) + \cos(\omega_+\tau)] \tag{7}$$

$$k(\theta) = \left(\frac{B\omega_I}{\omega_\alpha\omega_\beta}\right)^2 \tag{8}$$

The main shortcoming of the two-pulse experiment is that the primary echo decays with the phase memory time T_M which is often very short. This disadvantage can be avoided with the three-pulse ESEEM experiment shown in *Fig. 3,b*. In this pulse sequence, the first two $\pi/2$ pulses create nuclear coherence which evolves during the evolution time T and decays with the transverse nuclear relaxation time T_{2n}, which is usually much longer than the corresponding relaxation time T_M of the electrons. The third $\pi/2$ pulse transfers the nuclear coherence back to observable electron coherence. The modulation of the stimulated echo is given by *Eqn. 9*, with the contribution from the $\alpha(\beta)$ electron-spin manifold according to *Eqn. 10* (see *Fig. 2*). When T is varied, the echo envelope is modulated only by the two basic frequencies ω_α and ω_β, the sum ω_+ and difference ω_- frequencies do not appear, in contrast to the two-pulse ESEEM experiment. The three-pulse ESEEM amplitudes depend on τ which results in *blind spots* at $\omega_{\alpha(\beta)}$ when $\tau = 2\pi n/\omega_{\beta(\alpha)}$ ($n = 1, 2, \ldots$). As a consequence, the experiment often has to be performed with several τ values and spectra added to avoid blind-spot artifacts.

$$V_{3p}(\tau,T) = 1/2[V^\alpha(\tau,T) + V^\beta(\tau,T)] \tag{9}$$

$$V^{\alpha(\beta)}(\tau,T) = 1 - \frac{k}{2}[1 - \cos(\omega_{\beta(\alpha)}\tau)][1 - \cos(\omega_{\alpha(\beta)}(\tau + T))] \tag{10}$$

The four-pulse HYSCORE sequence (*Fig. 3,c*) is a 2D technique where an additional π pulse is introduced between the second and third $\pi/2$ pulse of the three-
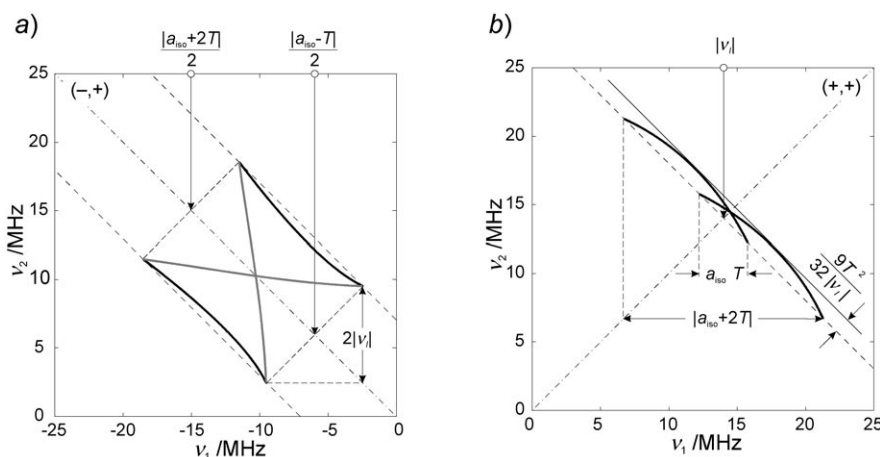
Fig. 4. *Theoretical HYSCORE powder patterns for an* $S=\frac{1}{2}$, $I=\frac{1}{2}$ *spin system with an axial hyperfine matrix:* a) *Strong-coupling case with* $\nu_I=3.5$ *MHz,* $a_{iso}=18$ *MHz and* $T=6$ *MHz* (black curves), $a_{iso}=2$ *MHz and* $T=14$ *MHz* (gray curves), b) *weak-coupling case with* $\nu_I=14$ *MHz,* $a_{iso}=2.5$ *MHz and* $T=6$ *MHz*

pulse ESEEM experiment. During the first evolution period t_1, the nuclear coherence created by the $\pi/2-\tau-\pi/2$ sub-sequence evolves in the $\alpha(\beta)$ electron-spin manifold. The nonselective π pulse interchanges the nuclear coherences between the electron-spin α and β manifolds. During the second evolution period t_2, the transferred nuclear coherence evolves in the $\beta(\alpha)$ electron-spin manifold, and a nuclear coherence transfer echo (CTE) is created at about time $t_1=t_2$ as a result of the refocusing of the hyperfine anisotropy [13]. Finally, the nuclear coherences are transferred to electron coherence by the last $\pi/2$ pulse and are detected as an electron-spin echo, which is modulated with the nuclear frequencies. For the two-spin system, cross-peaks can be observed at $(\pm\omega_a, \pm\omega_\beta)$ and $(\pm\omega_\beta, \pm\omega_a)$. If the modulation depth is small (*i.e.,* $2|\omega_I|\ll|A_S|$ or $|A_S|\gg2|\omega_I|$), nonideal m.w. pulses with an optimized strength and length can be used [14]. Spectra shown in *Figs. 10* and *Fig. 16* (see below) used matched m.w. pulses.

Fig. 4 shows typical HYSCORE powder patterns from an $S=\frac{1}{2}$, $I=\frac{1}{2}$ spin system. In the strong-coupling case, $|A_S|>2|\omega_I|$, the correlation ridges orient parallel to the diagonal and are separated by approximately $2|\omega_I|$. In the weak-coupling case, $|A_S|<2|\omega_I|$, the two arcs are displaced from the anti-diagonal at $|\omega_I|$, with a maximum frequency shift given by [15] (see *Eqn. 11*). The advantage of $\Delta\omega_{max}$ for inferring the anisotropic part of the hyperfine coupling arises from the fact that the intensities of the end points of the arcs vanish since they correspond to a depth parameter $k=0$ (*Eqn. 8*).

$$\Delta\omega_{max} = \frac{9}{32}\frac{T^2}{|\omega_I|} \tag{11}$$

2.5. Mims *and* Davies *ENDOR.* *Fig. 5* shows the *Davies* [16] and *Mims* [17] ENDOR pulse sequences. Both are based on the transfer of polarization between electron and nuclear transitions.
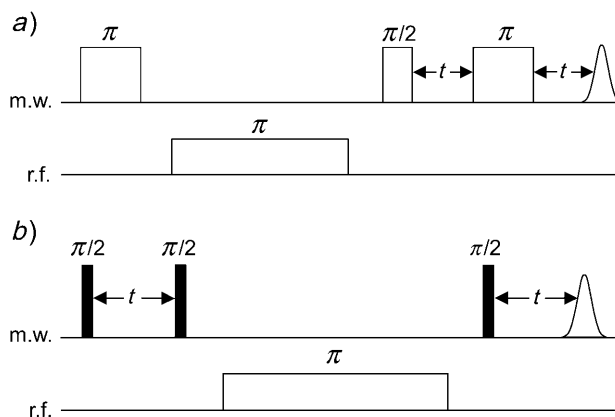
Fig. 5. *Pulse sequence for* a) Davies *ENDOR, and* b) Mims *ENDOR*. The inter-pulse delays are kept constant while the radio frequency is incremented over the desired frequency range.

In *Davies* ENDOR, the first selective m.w. π pulse inverts the polarization of a particular EPR transition (*Fig. 6,a* and *b*). Next, a selective r.f. pulse is applied. If the r.f. pulse is on resonance with one of the nuclear transitions (*Fig. 6,b* and *c*), the polarization of this transition is inverted, which also alters the polarization of the electron spin echo observer transition (1,3) which is detected *via* a primary echo, $\pi/2 - \tau - \pi - \tau$ echo. The ENDOR spectrum is thus recorded by monitoring the primary echo intensity as the r.f. is incremented stepwise over the desired frequency range.
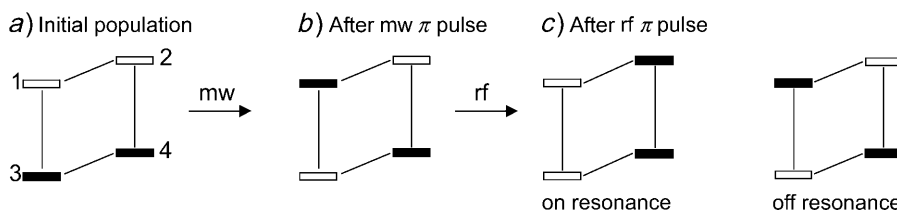

Fig. 6. *Populations of the energy levels of a two-spin system during the* Davies *ENDOR experiment:* a) *initial populations,* b) *selective m.w. π pulse inverts the polarization of EPR transition (1,3), and* c) *populations after the r.f. π pulse either on resonance with nuclear transition (1,2) or off resonance* (no effect)

Mims ENDOR is based on the stimulated echo sequence with three nonselective m.w. $\pi/2$ pulses (*Fig. 5,b*). The preparation part, $\pi/2 - \tau - \pi/2$, creates a τ-dependent grated polarization pattern. Next, the polarization is changed by a selective r.f. pulse if it is resonant with a nuclear transition. The electron polarization is then detected *via* a stimulated echo created at time τ after the last $\pi/2$ m.w. pulse. The ENDOR efficiency F_{ENDOR} is given by *Eqn. 12* [3] and depends upon the hyperfine coupling constant A_S and the time τ. It is maximum for $\tau = (2n+1)\pi/A_S$, and zero for $\tau = 2n\pi/A_S$, with $n = 0, 1, 2, ...$). *Mims* ENDOR thus exhibits a blind-spot behavior similar to three-pulse ESEEM and HYSCORE, but which now depends upon A_S (in three-pulse

ESEEM, the blind-spots depend upon ω_α and ω_β). Note that the deadtime of the spectrometer prevents very small τ values from being used (at X-band frequencies, typically τ is 100 ns or more). For $\tau = 100$ ns, blind spots occur when $A_S = 0, 10, 20, \ldots$ MHz. For large hyperfine couplings, it is thus usually preferable to employ the *Davies* ENDOR sequence with a well chosen length for the inversion π m.w. pulse [3]. On the other hand, *Mims* ENDOR can be particularly sensitive for measuring small hyperfine couplings if the phase memory time T_M of the sample is sufficiently long to allow an optimal τ value to be used.

$$F_{\text{ENDOR}} = \frac{1}{4}(1 - \cos(A_S\tau)) \tag{12}$$

2.6. *DEER Experiment with a Single Microwave Frequency.* DEER [18] is a technique to determine the mutual positions of unpaired electrons in rigid samples by measuring the electron–electron dipolar coupling (*Eqn. 2*). The technique can access electron–electron distances in the range $1-8$ nm. DEER is based on the separate excitation of two groups of electron spins by using two m.w. frequencies ω_{mw1} and ω_{mw2}. In the four-pulse variant shown in *Fig. 7,a*, the $\pi/2 - \tau_1 - \pi - \tau_1 - \tau_2 - \pi$ *refocused echo* sequence at frequency ω_{mw1} firstly creates $(\pi/2)$ and then doubly refocuses $(\pi - \tau_1 - \tau_2 - \pi)$ electron coherence. This coherence experiences a dipolar field B_{dd} due to the second group of electrons precessing at the frequency ω_{mw2}. Inversion of this dipolar field with a π-pulse at frequency ω_{mw2} causes an oscillation of the refocused echo as time t is varied with the frequency $\omega = g\beta_e B_{\text{dd}}$.

We have demonstrated that an independent excitation of two groups of spins can be achieved with a single m.w. frequency and a modulation of the static magnetic field B_0
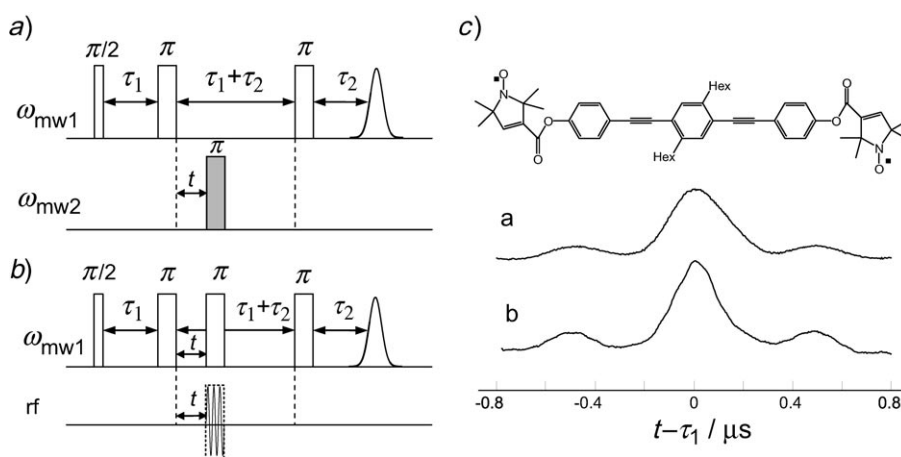

Fig. 7. a) *The standard DEER sequence with two m.w. frequencies, ω_{mw1} and ω_{mw2}.* b) *DEER with a 'bichromatic' pulse that excites a number of multiphoton transitions at frequencies $\omega_{mw1} \pm n\omega_{rf}$* c) *Comparison of four-pulse DEER time-traces obtained with two mw frequencies and with the bichromatic-pulse scheme on the sketched nitroxide biradical (standard four-pulse DEER 'a' with two m.w. frequencies, $\Delta\omega/2\pi = 24$ MHz, and four-pulse DEER with a bichromatic pulse 'b' with $\omega_{rf}/2\pi = 24$ MHz and $z \approx 2.4$; adapted from [19]).*

at the frequency $\omega_{rf} = (\omega_{mw1} - \omega_{mw2})$ [19]. Such 'bichromatic' irradiation excites a number of multiple photon transitions at frequencies $\omega_{mw1} \pm n\omega_{rf}$ ($n = 0, 1, 2, \ldots$). To illustrate the effect, consider the spin system described in a frame rotating at frequency ω_{mw} with the Hamiltonian of *Eqn. 13*, where $\Omega = \omega_S - \omega_{mw}$ is the resonance offset, and ω_1 and ω_2 are the amplitudes of the m.w. and modulation fields at frequencies ω_{mw1} and ω_{rf}, respectively. The eigenstates of the Hamiltonian, and possible transitions between them, can be found by removing the time dependence and using the rotation operator $\hat{R}(t) = \exp\left(i[n\omega_{rf}t + z\sin(\omega_{rf}t)]\hat{S}_z\right)$, where $z = 2\omega_2/\omega_{rf}$ and $n \in Z$. The resulting frame is known as the toggling frame, which has similarities to the rotating frame, but conveniently describes harmonics. In the toggling frame, *Eqn. 13* becomes *Eqn. 14*, where J_n is the *Bessel* function of the first kind of order n, and $O(t)$ describes oscillating terms. For $n = 0$ and neglecting $O(t)$, *Eqn. 14* describes *bare* spin states (the spin states without the B_0 modulation), for $n = \pm 1$, the eigenstates induced by the B_0 modulation are described. The longitudinal modulation not only disturbs the stationary-state energies, it modulates transition amplitudes as well. When $z = 2\omega_2/\omega_{rf} \approx 2.4$, the transition at frequency ω_{mw1} is *transparent*, but the spins with $\Omega_S = \pm 1\omega_{rf}$ will be excited effectively since $|J_{\pm 1}(z)|$ is close to its maximum value (*i.e.*, effectively we have a second m.w. frequency at $\omega_{mw1} \pm \omega_{rf}$).

$$\mathscr{H}_{SRF}(t) = \Omega_S \hat{S}_z + \omega_1 \hat{S}_x + 2\omega_2 \cos(\omega_{rf}t)\hat{S}_z \tag{13}$$

$$\mathscr{H}_{TF,n}(t) = (\Omega_S - n\omega_{rf})\hat{S}_z - J_n(z)\omega_1 \hat{S}_x + O(t) \tag{14}$$

This method was successfully applied to DEER experiments [19] as shown in *Fig. 7,b*, where the second m.w. frequency ω_{mw2} is in essence created with a 'bichromatic' pulse with frequency ω_{mw1} and ω_{rf}. *Fig. 7,c* shows the dipolar oscillations obtained by using this sequence and conventional DEER, the concurrence is excellent. The transparency condition ($z \approx 2.4$) was also verified experimentally by generating a primary electron-spin echo (*Fig. 3,a*) with a single long m.w. pulse and a slightly shorter r.f. pulse positioned between the m.w. pulse to create transparency and thus an effective τ time [20]. Soft ESEEM-type experiments, which require two coherent m.w. sources, can also be realized with bichromatic pulses [19].

2.7. *Simulation of EPR Spectra.* EPR Spectra (CW EPR, ENDOR, and ESEEM) can rarely be analyzed quantitatively by visual inspection alone. To extract magnetic and structural parameters requires numerical simulations of the experimental EPR spectra. We have developed a software package, EasySpin [21], that can simulate a wide range of EPR spectra. This program runs under Matlab and is freely available [22]. The following discusses some relevant aspects implemented in the program and of EPR simulations in general.

For isotropic CW-EPR spectra, such as obtained from fast-tumbling organic radicals in solution, the spectral simulation is straightforward. Anisotropic interactions are averaged out, only allowed EPR transitions are visible, and their intensities are all equal. To compute the resonance-line positions, the analytical *Breit–Rabi* expression for the energy levels as a function of the external field B_0 is solved for B_0 by using a fixed-point iteration [21]. This novel method is superior to the commonly used pertur-

bation-theory solutions, since it converges to the exact resonance field within numerical accuracy after two to three iterations, even for very large hyperfine couplings.

In single crystals, powders, and frozen solutions, paramagnetic centers are immobilized. Their CW-EPR spectra feature the full anisotropy of all magnetic parameters. Resonance-line positions depend on the orientation of the paramagnetic center with respect to $\mathbf{B}_0$. For paramagnetic centers containing transition metals, the dependence of the energy levels on $\mathbf{B}_0$ can be quite complex. It is, therefore, no easy endeavor to compute the resonance-line positions of a general spin system. We have developed a robust method that adaptively models the field dependence of the energy levels using cubic splines to obtain accurate resonance-line positions [23]. In this method, the number of spin Hamiltonian diagonalizations automatically adapts to the complexity of the spin system. For a disordered system, resonance-line positions and intensities have to be computed for a large number N of orientations and then summed up. The time needed to simulate the overall EPR spectrum is directly proportional to the minimum N needed to construct a smooth powder spectrum, commonly several thousand. If N is too small, the spectrum features computational artefacts in the form of oscillations. We apply a projective technique [21] that, instead of a discrete summation, uses a series of semi-continuous projections combined with interpolation to obtain the powder spectrum. In this way, N can be reduced by an order of magnitude compared to the standard summation approach.

In addition to the isotropic and the rigid limit described above, EasySpin contains functionality for simulating CW-EPR spectra in the fast and slow motional regimes [24] based on *Redfield* theory and the stochastic *Liouville* equation.

In comparison to CW EPR, the simulation of ENDOR spectra is simple. For a given orientation of the paramagnetic center, peak positions are obtainable as differences of the energy eigenvalues of the spin Hamiltonian at the given magnetic field. Peak intensities for CW ENDOR are equally simple [20]. For pulse ENDOR spectra, usually the CW-ENDOR intensities are used. In this case, care must be taken, *e.g.*, the blind spots in *Mims* ENDOR need to be considered.

The simulation of ESEEM spectra is by far the most challenging. Although the underlying theory appears to be well known [3], a general and robust simulation approach yielding spectra that quantitatively reproduce experimental ones is still lacking. ESEEM Frequencies can usually be computed reliably, but accurate peak intensities in disordered systems are often elusive. One of the main problems is that peak intensities are associated with a complex phase. Destructive phase-interference effects have a large influence on the computed spectrum, and are most pronounced in samples containing inhomogeneous broadening [25]. Inhomogeneous broadening arises from orientational distributions, and distributions in the g values, hyperfine couplings, and nuclear quadrupole couplings of the system. As a result, even peaks with only a small inhomogeneous broadening have intensities that strongly deviate from the ones without such a broadening. Another aspect that has not yet received appropriate attention is the proper treatment of detection. Although most spectra are measured by using a boxcar detection window centerd on the spin echo, they are nonetheless simulated assuming a single-point detection at the echo maximum. Since the boxcar detector acts as a filter, its bandwidth-limiting effect on simulated spectra must be carefully accounted for. In multinuclear spin systems, it is an unfortunate fact that nuclei causing

deep modulations significantly suppress peaks from nuclei with weak modulations. This cross suppression effect [26] implies that, for a proper simulation of a spectrum, all nuclei that contribute to the spectrum have to be included.

Apart from modelling the experimental conditions correctly, there can also be time-consuming bottlenecks depending upon the computational method employed. For the simulation of a HYSCORE spectrum of a disordered system, nuclear coherences have to be evolved in time for every orientation to obtain the full-time trace. The resulting simulation times can be exacting. By performing the simulation in the frequency domain instead of the time domain, interpolation and filter techniques can be used to reduce computational times by up to two orders of magnitude [27].

Ultimately, one would like to fit all experimental spectra simultaneously with simulations of both the frequencies and intensities in a global fashion. This would provide the most accurate and robust parameter estimates, and statistically significant errors can be given.

3. Applications. – 3.1. *Porphyrin Derivatives.* There is no doubt that porphyrin derivatives belong to the most intensively studied systems in coordination chemistry [2]. A myriad of porphyrin-like macrocycles have been isolated or synthesized, and their metal complexes continue to attract the attention of researchers all over the world working in different fields from biology to materials science.

3.1.1. *Copper(II) Complex of N-Confused Tetraphenylporphyrin.* A relatively new member of the porpyhrin family is the N-confused porphyrin (ncp), also known as 'inverted' porphyrin, whose detection was first reported independently by two groups in 1994 [28][29]. This porphyrin isomer retains the molecular backbone of the regular porphyrin but contains a confused pyrrole ring connected through its α,β'-positions (*i.e.*, C(2) and C(4); pyrrol numbering) in the macrocycle with one pyrrole H-atom (H−C(3)) pointing into the cavity (*Fig. 9*, inset). For recent reviews, see [2][30–32].

Initially, the ncp was isolated as a by-product with yields between 5 and 7%. In the late 1990s, *Lindsey* and co-workers [33] optimized the synthesis to obtain yields of up to 37% of the N-confused tetraphenylporphyrin (=2-aza-5,10,15,20-tetraphenyl-21-car-baporphyrin; nctpp) by using the one-flask condensation of pyrrole and benzaldehyde in the presence of the methanesulfonic acid catalyst. N-Confused porphyrins form stable organometallic complexes with many transition-metal centers [2]. Important is the macrocycle's ability to act as a neutral to trianionic ligand. Coordination to the 'outer' N-atom has also been observed [34]. The ligand can stabilize uncommon spin and oxidation states of various metal ions thereby forming a C−metal bond. One of the first compounds investigated by CW-EPR spectroscopy was the complex (N-confused tetra-phenylporphyrinato)copper(II) ([Cu^{II}(nctpp)]) [35][36] for which a remarkable deviation from the spectral parameters of (tetraphenylporphyrinato)copper(II) ([Cu^{II}(tpp)]) was found (*Fig. 8*). These findings stimulated our multi-frequency (X-, Q-, and W-band) CW- and pulse-EPR study of this compound, the aim of which was to determine the electronic structure in detail and to compare the results to the symmetric [Cu^{II}(tpp)] complex [37]. From an analysis of the CW-EPR spectrum, the existence of two different N-atom hyperfine couplings along $g_{\parallel}$ can be deduced. The spectrum could only be simulated assuming two N-atoms with hyperfine values $A_{\parallel}^{N(1),N(2)} \approx 59$ MHz and one N-atom with $A_{\parallel}^{N(3)} \approx 29.5$ MHz (*Fig. 8*, lower inset). Nevertheless, the full hyperfine coupling
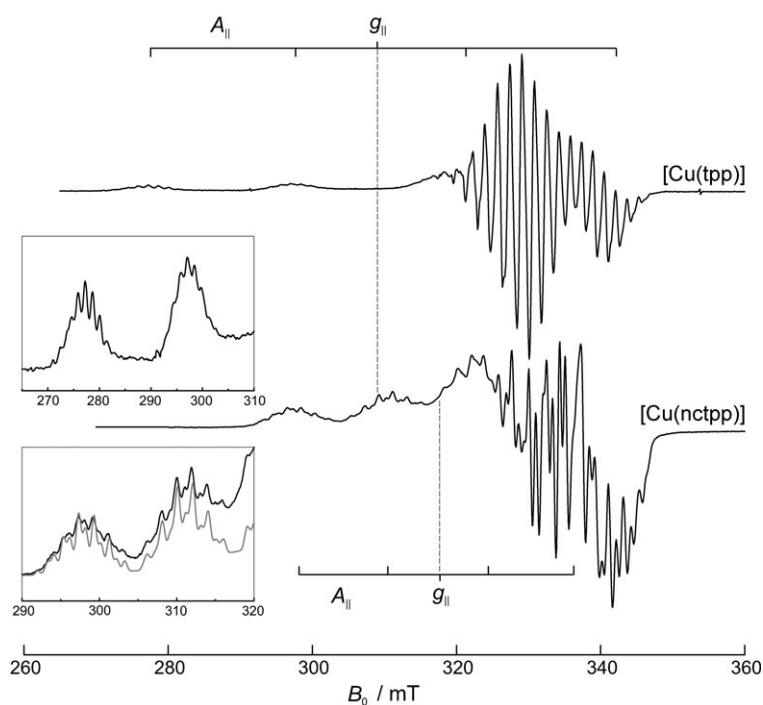
Fig. 8. *Comparison of the CW-EPR spectra of [Cu^{II}(tpp)] and [Cu^{II}(nctpp)], diluted in [Zn(tpp)] powder, recorded at 150 K.* The shifts of $g_{||}$ and the corresponding copper hyperfine interactions $A_{||}$ to lower values for [Cu^{II}(nctpp)] are clearly visible. The insets show a magnification of the low-field region depicting the additional splitting caused by the directly coordinating N-atoms. Adapted from [37].

tensors cannot be derived from the CW spectrum. Pulse methods performed at different observer positions allow for an accurate determination of these values.

Fig. 9 shows the Q-band *Davies* ENDOR spectra measured close to $g_{||}$ (*Fig. 9,a*) and at the echo maximum around $g_{\perp}$ (*Fig. 9,b*). The spectrum recorded at $g_{||}$ consists of a *doublet* split by $2\nu_N$ and centred around $\nu_{rf} = 30$ MHz. Therefore, this signal is assigned to strongly interacting core N-atoms of the porphyrin macrocyle. The nuclear quadrupole splitting along this orientation is unresolved, whereas it is clearly visible upon changing the observer position to $g_{\perp}$.

The interactions arising from the third core N(3) and the 'outer' N(4) nuclei could be clearly observed with HYSCORE spectroscopy at Q-band frequency. *Fig. 10* shows the HYSCORE spectra measured at $g_{||}$ and the resulting narrow peaks due to the small number of contributing orientations (single-crystal-like position). The peaks in the $(-,+)$ quadrant (*Fig. 10,a*) correspond to strong hyperfine couplings which consequently can be assigned to the third core N-atom. The spectrum shown in *Fig. 10,b* results from weak hyperfine coupling and, therefore, originates from the 'outer' N-atom located in the confused pyrrole ring.

The detailed results for the core N-atoms confirmed the findings based on the analysis of the CW data. In [Cu^{II}(nctpp)], the hyperfine interactions arising from the core

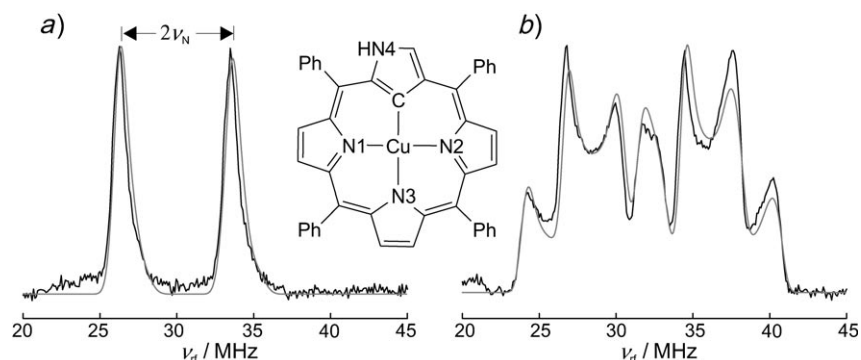Fig. 9. *Q-Band* Davies *ENDOR spectra* (20 K) *of [Cu^{II}(nctpp)] diluted in [Zn(tpp)] powder measured at two different observer positions.* Black traces, experiments; gray traces, simulations. The hyperfine and the nuclear quadrupole interaction of these strongly interacting N-atoms increase upon changing the observer position from *a*) $g_{\parallel}$ to *b*) $g_{\perp}$. Adapted from [37].
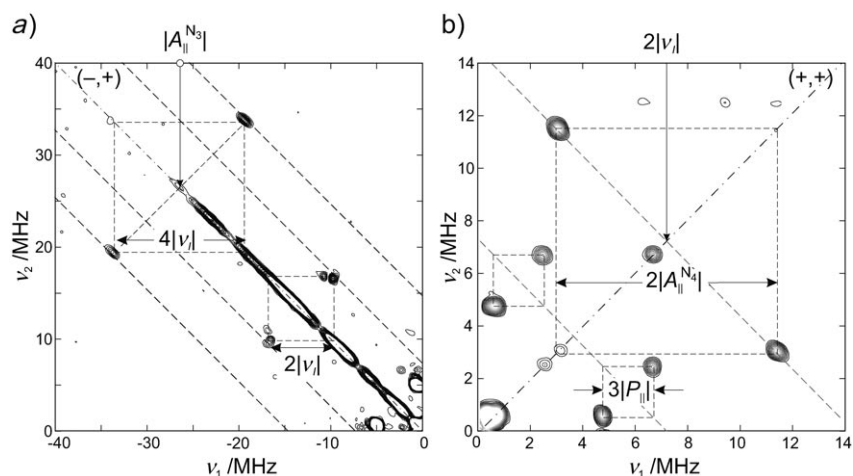

Fig. 10. *Matched Q-band HYSCORE spectra* (20 K) *of [Cu^{II}(nctpp)] diluted in [Zn(tpp)] powder; observer position at* $g_{\parallel}$. For clarity purposes, the $(-,+)$ and $(+,+)$ quadrants use different scales. *a*) shows the third core N-atom with a hyperfine interaction $A_{\parallel}^{N(3)}$ smaller than the one observed in [Cu^{II}(tpp)], whereas *b*) shows the interactions $A_{\parallel}^{N(4)}$ caused by the 'outer' N-atom of the confused pyrrole ring. Along this orientation, the parameters can be directly read out from the spectrum. Spectra and the corresponding simulations from other B_0 observer positions (not shown here) enabled an accurate determination of the magnetic interactions. Adapted from [37].

N-atoms are no longer equivalent, in contrast to the situation in [Cu(tpp)]. More specifically, one of the N-atoms exhibits a hyperfine coupling which is approximately half as large as the other two, indicating an asymmetric spin-density distribution over the complex. This finding is in excellent agreement with results derived from density-functional-theory (DFT) calculations [37].

　　This example nicely shows how pulse EPR techniques can obtain a detailed picture of the asymmetric spin-density distribution on the macrocycle. By applying similar
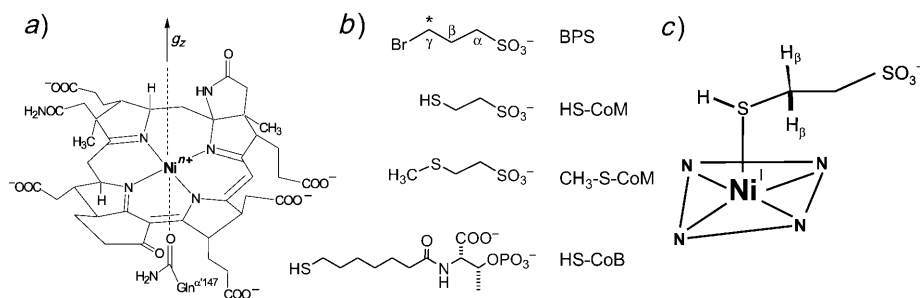
Fig. 11. a) *Schematic representation of F_{430}* (for Ni^{III}: $n=2$) *and the direction of the* g_z *axis;* b) *substrates or substrate analogues: BPS* (3-bromopropane-1-sulfonate; *the asterisk marks the position of the* [13]C-*isotope labeling*); *HS−CoM* (coenzyme M (reduced)); *CH₃−S−CoM* (methyl-coenzyme M), *and HS−CoB* (coenzyme B), *and* c) *sketch of the proposed coordination geometry in* MCR_{red2}

techniques, other important issues can be addressed, *e.g.*, the protonation state of the outer N-atoms or the character of the metal−C interaction arising from the confused pyrrole ring. These are currently under investigation in our laboratory.

3.1.2. *Alkyl– and Sulfur–Nickel Bonds in Methylcoenzyme M Reductase.* Methyl-coenzyme M reductase (MCR) catalyzes the reduction of methylcoenzyme M (CH₃−S−CoM) with coenzyme B (HS−CoB) to methane and the heterodisulfide CoM−S−S−CoB in methanogenic archaea (*Fig. 11*). All methanogens contain MCR, and X-ray crystallography of inactive Ni^{II} forms shows that the enzyme has two identical active sites, each containing one molecule of cofactor F_{430}, an Ni-containing porhyrinoid [38][39]. In the active state, designated MCR_{red1}, the central metal is in the Ni^I valence state, and its EPR spectrum is characteristic of a d^9 $S=\frac{1}{2}$ species with the unpaired electron in a molecular orbital of predominantly $d_{x^2-y^2}$ character [40].

We have investigated several species that are induced in the presence of substrate analogues or inhibitors such as (reduced) coenzyme M (2-mercaptoethanesulfonate; HS−CoM) [41–43] or 3-bromopropane-1-sulfonate (BPS) [44]. Note that both Ni−C [45] and Ni−S [46a,b][4]) coordinated complexes are intermediates in proposed catalytic cycles for MCR. In particular, HYSCORE and pulse ENDOR techniques were employed to address the question whether CoM and BPS form chemical bonds to the Ni ion of F_{430}. In this section, we discuss three species: MCR_{ox1} which is induced under (relative) oxidizing conditions in the presence of CoM; MCR_{red2} which is induced when CoM and CoB (= *N*-(7-mercapto-1-oxoheptyl)-L-threoninate *O*-phosphate) are added to MCR_{red1} [42][43]; and MCR_{BPS} which is induced when BPS is added to MCR_{red1}.

MCR_{ox1} and MCR_{BPS} species have *g* values that are indicative of a singly occupied molecular orbital (SOMO) with high $d_{x^2-y^2}$ character (*Table 1*). The *g* values of MCR_{red2} are striking, they are highly orthorhombic with a relatively small anisotropy, and are shifted to higher values. This is a clear indication of a significant geometric or electronic distortion of the marcocycle F_{430}. To aid the elucidation of the axial bonding situation in

---

[4])   On the difficulties of calculating transition-metal−C bond energies by means of DFT, see [46c].

Table 1. *MCR$_{ox1}$, MCR$_{red2}$, and MCR$_{BPS}$ Hyperfine and Nuclear Quadrupole Parameters. A_i and $|e^2qQ|/h$ are in MHz.*

	g_x, g_y, g_z	Atom	$|A_x|, |A_y|, |A_z|$	$|e^2qQ|/h$	η
MCR$_{ox1}$	2.153, 2.168, 2.231	^{33}S	10, 24, 17	36	0.1
		^{14}N (×4)	23−36	2.9−3.5	0.12−0.21
MCR$_{red2}$	2.287, 2.231, 2.175	^{33}S	15, 15, 35	–	–
		^{14}N (×3)	20−27	2.0−2.5	0.0−0.2
		^{14}N (×1)	16.0, 13.5, 11.8	2.4	0.15
MCR$_{BPS}$	2.108, 2.112, 2.219	^{13}C$_\gamma$	17.6, 18.3, 45.0	–	–
		^{14}N (×4)	23−34	2.4−3.6	0.3−0.7

the three different species, isotope labeling was used to obtain (^{33}S)CoM [41][42], and (^{13}C)BPS [44].

Fig. 12,a and *b* display two representative Q-band HYSCORE spectra from MCR$_{ox1}$ with the substrate (^{33}S)CoM. The spectra contain cross-peaks that stem from ^{33}S single-quantum ($\Delta m_I = \pm 1$) and double-quantum ($\Delta m_I = \pm 2$) transitions, which were analyzed to obtain the ^{33}S hyperfine and nuclear quadrupole coupling parameters. The simulation (*Fig. 12,c*) of the spectrum shown in *Fig. 12,a* was performed with the parameters given in *Table 1*. The HYSCORE spectrum recorded at the high-field end
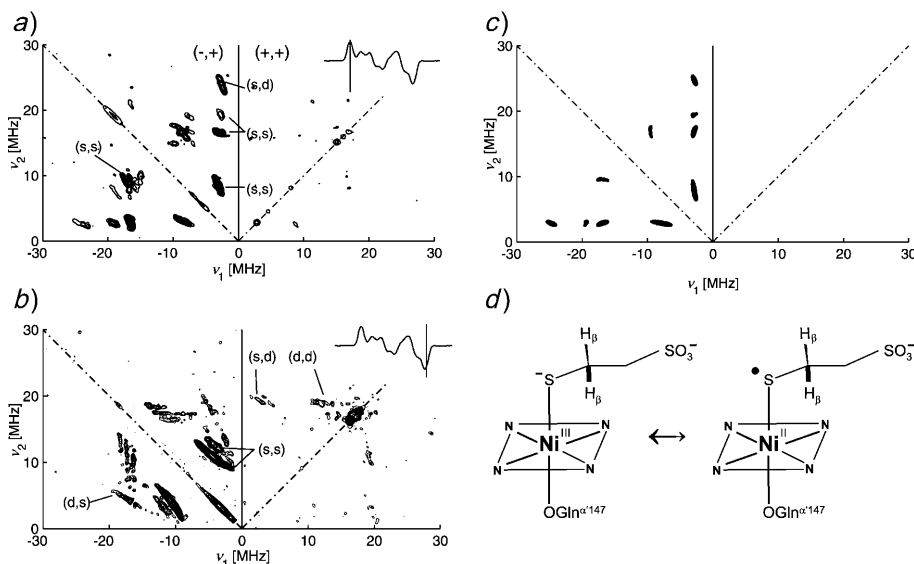

Fig. 12. *Q-Band* (35.26 GHz) *HYSCORE spectra of [(^{33}S)CoM]−MCR$_{ox1}$ measured at 25 K at* a) *the extreme-low and* b) *high-field positions of the EPR spectrum* (both spectra are the sum of two τ values, 108 ns and 132 ns; selected ^{33}S double-quantum (d) and single-quantum (s) frequencies are labelled; insets: echo-detected EPR spectra (first derivatives) indicating the observer positions of the HYSCORE spectra). c) *Simulation of the frequency positions of 'a'.* d) *Proposed electronic structure of MCR$_{ox1}$.* Figures adapted from [41].

of the EPR spectrum (*Fig. 12,b*) has intense (s,s) cross-peaks that form two long ridges in the (−,+) quadrant. The doubling of the ridges is caused by the nuclear quadrupole splitting, whereas the length is determined by the anisotropy of the ^{33}S hyperfine interaction. Positions and lengths of these two pairs of ridges thus provide initial values for the hyperfine couplings in the $\mathbf{g}_x - \mathbf{g}_y$ plane, $A = 10 - 20$ MHz. In both spectra, the most intense peaks occur in the (−,+) quadrant, indicating that at Q-band, the ^{33}S hyperfine interaction is in the strong coupling regime, $|A_S| > 2|\omega_I| = 7.5$ MHz.

The ^{33}S hyperfine coupling allows an estimation of the spin population at the ^{33}S atom of *ca.* 7%, it can thus be safely deduced that a chemical bond between Ni and the thiolate S-atom of $^-$S−CoM is formed. The proposal for the electronic structure is given in *Fig. 12,d*, a (thiolato)nickel(III) (d^7) in resonance with a thiol radical/ high-spin Ni^{II} complex, Ni^{III}−$^-$SR ⇌ Ni^{II}−˙SR.

MCR$_{BPS}$ exhibits a Ni−alkyl bond which results from the nucleophilic attack of MCR$_{red1}$ on the C(γ) atom of BPS (Br$^-$ leaves BPS). This is the first account of a transition-metal−alkyl derivative found in an enzyme in which the alkyl group is not bound to cobalt [44]. *Fig. 13,a* shows Q-band *Davies* ENDOR spectra from MCR$_{BPS}$ (the control) and ^{13}C-MCR$_{BPS}$ measured at the two field positions highlighted in the echo-detected field-swept EPR spectrum shown in *Fig. 13,b*. The simulations by means of the hyperfine couplings given in *Table 1* are shown as dashed lines. The ^{13}C(γ) hyperfine couplings were extracted from both *Davies* ENDOR and HYSCORE measurements at Q-band. These data establish that there is a bond between the Ni of F$_{430}$ and the C(γ) of the propanesulfonate moiety, with *ca.* 7% of the spin population being in a predominately p-type C(γ) orbital. The data resolution was high enough to determine that the Ni−C(γ) axis is tilted away from the axial position by *ca.* 20° (see *Fig. 13,c*). Together with information derived from the measured proton hyperfine couplings at X-band, it can be assumed that the geometry at the alkyl center is flattened and the hybridization is closer to sp^2 than sp^3. MCR$_{BPS}$ is formally best described as an alkyl−Ni^{III} complex [44].

MCR$_{red2}$ is a Ni^I species [42][43], and Q-band HYSCORE was again used to show that the S-atom of HS−CoM is coordinated to the Ni-ion [43]. An intriguing difference between this species and MCR$_{red1}$, MCR$_{BPS}$, and MCR$_{ox1}$ is the large inequivalence of the hyperfine couplings of the four N-atoms in the hydropyrrole rings of F$_{430}$ (see *Table 1*). This result suggests that there is a significant electronic or geometric distortion of the cofactor F$_{430}$ (see *Fig. 11,c*).

3.1.3. *Heme Groups in Proteins.* The heme group is a (porphyrinato) iron complex that is found in nature as a cofactor in many proteins. Heme proteins perform different functions in a great variety of organisms such as O$_2$ transport, detoxification, electron transport, and catalysis. The heme group can be found in diverse states of oxidation and spin, and in environments of different symmetry. The SOMO of the Fe heme is very sensitive to its local environment, making it a good structural probe. Moreover, as many of the functions of hemoproteins utilize a redox reaction involving the cofactor, knowledge of the spin-density distribution can help to unravel the mechanism and to understand their versatile functionality. The study of hemoproteins by EPR has a long history. In particular, the analysis of CW-EPR spectra by means of the hole model of *Griffith* [47] provides information about the SOMO and the nature and spatial arrangement of the axial ligands. The presence of magnetic nuclei in the immediate
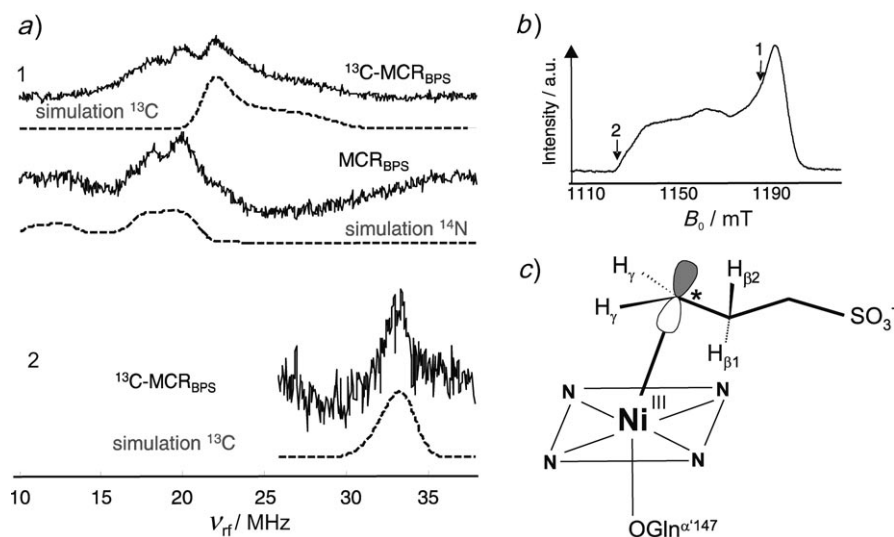
Fig. 13. *Q-band* (*ca.* 35.3 GHz) *EPR experiments with* (*^{13}C*)*MCR*$_{BPS}$ *and MCR*$_{BPS}$: a) 1 *Davies ENDOR spectrum from* (*^{13}C*)*MCR*$_{BPS}$ (upper solid line), *simulation of the* *$^{13}C(\gamma)$-signals* (upper dashed line)*, and spectrum of MCR*$_{BPS}$ (lower solid line) *and simulation of the hydropyrrole* *^{14}N* *atoms of F*$_{430}$. 2 *spectrum from* (*^{13}C*)*MCR*$_{BPS}$ *and simulation of the* *$^{13}C(\gamma)$-signals* (MCR$_{BPS}$ does not display signals at this observer position; only the high-frequency peaks are shown). b) *Echo-detected field-swept EPR spectrum of* (*^{13}C*)*MCR*$_{BPS}$ (arrows marked with '1' and '2' show the field positions of the Davies ENDOR spectra). c) *Schematic structure of MCR*$_{BPS}$. Figures adapted from [44]

heme environment provides probes to explore the unpaired-electron-spin distribution in the molecule using ENDOR or ESEEM techniques.

Pulse EPR was used to study cytochrome b_{559} (cyt b_{559}) which is present in the tylacoid membranes of green plants [48]. This protein contains a bis-histidine coordinated heme and consequently, the Fe-ion is bound to six N-atoms, four from the heme and two from the axial histidine ligands, all of which potentially contribute to the spectra. To help in the analysis of cyt b_{559}, the complex [Fe^{3+}(ppIX)(im)$_2$] was used as a model (ppIX = protoporphyrin IX, im = 4-methyl-1H-imidazole; *Fig. 14,a*) since its spectra (from CW-EPR and ESEEM measurements) were very similar to those of the protein. The complex was selectively labeled with ^{15}N either in the porphyrin or in the axial imidazole ligand thereby allowing the assignment of the signals to the various coordinating N-atoms. *Fig. 14,b* shows a HYSCORE spectrum from [Fe(ppIX)(im)$_2$] which contains cross-peaks from three different pairs of N-atoms that interact with the unpaired electron spin. By combining the data from spectra taken at several field positions, the hyperfine and nuclear quadrupole tensors of every N pair were determined. These tensors and the results from an analysis of the CW-EPR spectra enabled the orientation of the two parallel axial imidazole ligands with respect to the porphyrin ring to be established. The ligand spin densities and g values allowed the spatial distribution of the SOMO to be inferred which indicates that the spin density is localized on the Fe-ion.
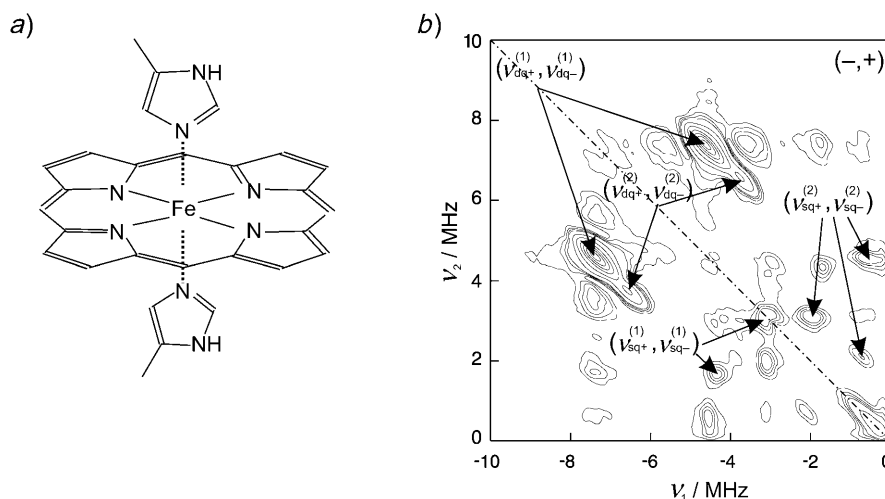
Fig. 14. a) *Sketch of the complex [Fe^{III}–(ppIX)(im)$_2$] showing the macrocycle protoporphyrin IX and the imidazole ligands.* b) *X-Band HYSCORE spectrum of the model complex [Fe^{III}(ppIX)(im)$_2$]. B_0 is oriented in the direction perpendicular to the porphyrin plane. Labeled with (1) are the signals corresponding to the heme N-atoms, with (2) the imidazole N-atoms.*

3.2. *Aminyl Radicals Stabilized by Rhodium.* Free aminyl radicals, $R_2N^{\cdot}$, or amine radical cations, $R_3N^{\cdot+}$, play an important role in many chemical [49] and biological processes [50]. Generally, these radicals are highly reactive short-lived intermediates with lifetimes in the micro- to millisecond range, and are formed thermally or photolytically by homolytic bond cleavage or by redox reactions. Relatively persistent aminyls (*Scheme, a*, **I**) are obtained when the spin density is delocalized in a conjugated π-system, and/or an adjacent donor group Y with a lone pair of electrons in a π-type orbital is bonded to the formally electron-deficient N-atom. When sufficiently bulky substituents are introduced, aminyls can be isolated [51], and 2,2-diphenyl-1-picrylhydrazyl (=DPPH; R=NO_2, Y=Ph_2N) is a prominent example of this strategy.

Scheme. a) *Concepts to Stabilize Aminyl Radicals.* b) *Spherically Delocalized Non-Innocent Ligand Complex* **III** *and Centrally Metal-Delocalized Radical Complex* **IV**.
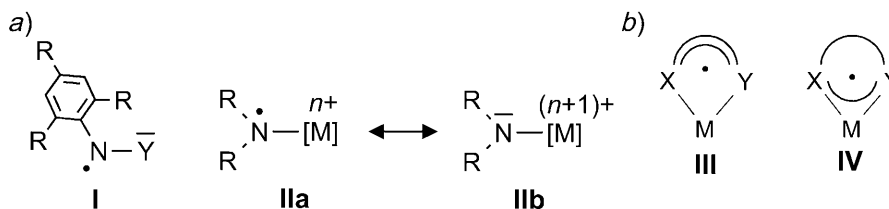
Electron-rich transition-metal fragments should be likewise efficient as stabilizing groups. d^8-Rh^I-containing fragments are especially suited because the metal serves as an electron donor *via* one of the filled d_{xy}, d_{xz}, or d_{yz} orbitals. Limiting resonance forms to the electronic ground state of an aminyl-radical complex may be $[M]^{n+}$–

N$\cdot$R$_2$ (**IIa**) or [M]$^{(n+1)+}$−N$^-$R$_2$ (**IIb**) (*Scheme, a*). In most cases, this latter metal amide form is the better description, *i.e.*, the unpaired electron is mainly localized at the metal center [52]. Complexes with the spin predominantly localized at the N-atom, as in **IIa**, are rare [53]. Here, we present two complexes where an aminyl radical(s) could be stabilized by coordination to a Rh-metal (*Scheme, a*, **IIa**).

Fig. 15,a shows the structure of the trigonal bipyramidal cationic complex [Rh(trop$_2$N$\cdot$)(bipy)]$^+$, which has a coordinatively saturated Rh^I center with a formal 18-electron configuration (trop$_2$NH = N-(5H)-dibenzo[a,d]cyclohepten-5-yl)-5H-dibenzo[a,d]cyclohepten-5-amine, bipy = 2,2′-bipyridine) [54]. The electronic structure was determined in detail by EPR spectroscopy. In solution, the compound shows a well resolved CW-EPR spectrum (*Fig. 15,b*) that was simulated by using isotropic couplings from the atoms N(1) and N(2), Rh, and the two benzylic protons. The anisotropic parts of the hyperfine couplings were determined in frozen solution from ENDOR and HYSCORE spectroscopy (*Fig. 15,d*). *Table 2* contains EPR parameters for Rh and N(1), where the spin density is predominantly located. Of particular significance is the large N hyperfine coupling of N(1), which equates to a spin population of $57 \pm 4\%$. This result is supported by DFT calculations, which gave a spin density of 56% on N(1) and 30% on Rh. The complex is thus best described as an aminyl-radical complex [Rh^I(trop$_2$N$\cdot$)(bipy)]$^+$OTf$^-$, and not as an aminatorhodium(II) complex [Rh^{II}(trop$_2$-N$^-$)(bipy)]$^+$OTf$^-$.

Table 2. *Spin Populations ρ and EPR Parameters of the Two Aminyl Complexes.* DFT Values are given in italics. A_i, a_{iso}, and T are expressed in MHz.

	[Rh(trop$_2$N$\cdot$)(bipy)]$^+$ [54] $g_{iso}=2.0512$, $g_1=2.0822$, $g_2=2.0467$, $g_3=2.0247$				[Rh(trop$_2$dach$-$2H)]$\cdot$ [55] $g_{iso}=1.996$, $g_1=2.005$, $g_2=1.992$, $g_3=1.991$			
	ρ [%]	A_1, A_2, A_3	a_{iso}	T	ρ [%]	A_1, A_2, A_3	a_{iso}	T
Rh	–	12, 18, 48	26.8	−14, −8, 22		6.0, 4.6, −13.3	−0.9	6.9, 5.5, −12.4
	30	*0, 13, 35*	*16*	*−16, −3, 19*	*41*	*−44, −47, −76*	*−57*	*12, 10, −22*
N	57	18, 18, 98	45.1	−26.7, −26.7, 53.3		−1.9, −1.9, 37.0	11.1	−12.9, −12.9, 25.9
	56	*3, 3, 84*	*31*	*−27, −26, 53*	*56*	*−1, −1, 38*	*12*	*−13, −13, 26*

The second compound discussed here demonstrates that an aminyl radical can also be stabilized by an adjacent tetracoordinated formally 16-electron Rh^I fragment, see *Fig 16,a* [55]. The stability of the radical [Rh(trop$_2$dach$-$2H)]$\cdot$ is sufficient to allow it to be oxidized by ferrocenium triflate and thus studied by EPR (trop$_2$dach = (R,R)-N,N'-bis(5H-dibenzo[a,d]cyclohepten-5-yl)cyclohexane-1,2-diamine). Its X-band CW-EPR spectrum in Et$_2$O at 298 K is shown in *Fig. 16,b*, and yields, after simulation, the isotropic hyperfine couplings attributed to the aminyl N, the H$_\beta$, and the H$_{bz}$ atoms. *Fig. 16,d* shows a representative HYSCORE spectrum that contains both N and Rh signals. The long ridges assigned to the N-atoms result from the large anisotropy of the hyperfine interaction, and their splitting into two sets is the result of the nuclear quadrupole interaction. Signals from Rh form part of a cross, with the splittings at the edges allowing the principal values of the nearly axial hyperfine interaction to be evaluated (see also *Fig. 4,a*, grey line).
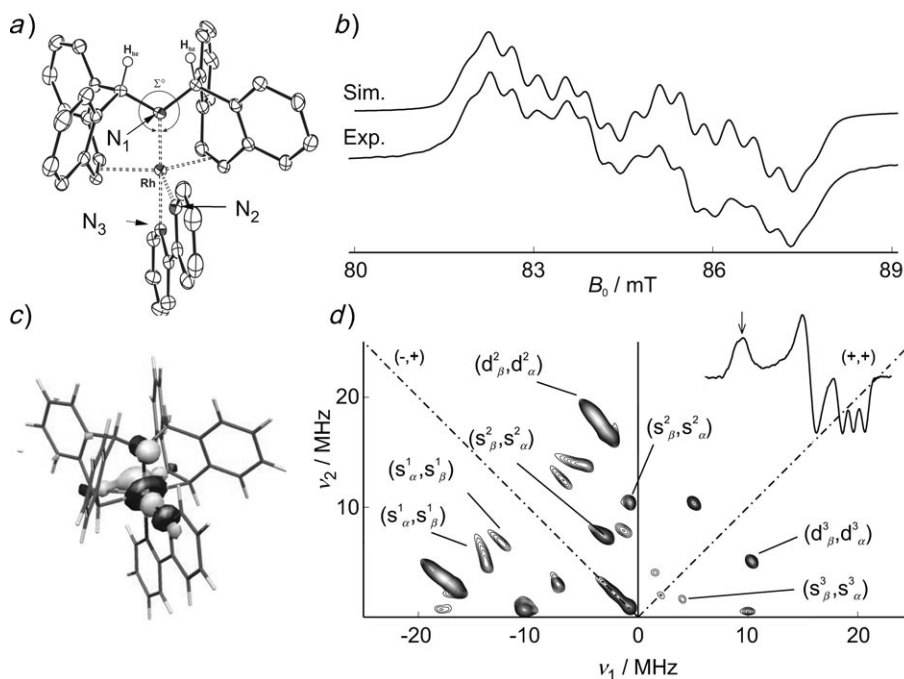
Fig. 15. a) *X-Ray structure of [Rh^I(trop$_2$N$^\bullet$)(bipy)]$^+$ showing the N-atom labelling* (H-atoms, apart from the two benzylic ones (H$_{bz}$), and the CF$_3$SO$_3^-$ anion are omitted). b) *S-Band CW-EPR spectrum at room temperature in THF/acetone, experimental* (Exp.) *and simulated* (Sim.). c) *Plot of the SOMO.* d) *Q-Band HYSCORE spectrum measured at 25 K at observer position* g$_I$ (the cross-peaks are assigned to the three N-atoms (identified by the superscript 1, 2, or 3 as defined in *a* by N$_1$, N$_2$, and N$_3$), some of the double-quantum (d) and single-quantum (s) frequencies in the α and β electron-spin manifolds are labelled). Figures adapted from [54].

The experimentally derived parameters for Rh and the aminyl N-atoms are given in *Table 2*, along with the data calculated by DFT. According to the calculations (*Fig. 16,c* shows the SOMO), the main part of the spin population is located on the two aminyl N-atoms (28% ×2) and the Rh-center (41%). The unpaired electron is thus centrally delocalized over the metal center, in contrast to the well-studied complexes **III** (*Scheme*, *b*) with 'noninnocent' ligands[5]) X∩Y where the unpaired electron is delocalized in the conjugated ligand sphere. This concept allows the synthesis of rather persistent metal-coordinated radicals.

Both radical complexes have remarkably low oxidation potentials as compared to amines (NR$_3$ − e$^-$ → NR$_3^{\bullet+}$; E°(irreversible): +0.4 to +1.3 V (*vs.* Fc/Fc$^+$)). The complex [Rh^I(trop$_2$dach − 2H)]$^-$ shows two reversible oxidation waves at −1.02 and −0.38 V, and [Rh^I(trop$_2$N)(bipy)] one oxidation at −0.55 V. The radical complexes were tested for their H-abstraction reactivity with substrates of varying H-donor ability. For exam-

---

[5]) There is a vast quantity of literature on this topic which is impossible to provide here; see the selected references and literature cited in [56].
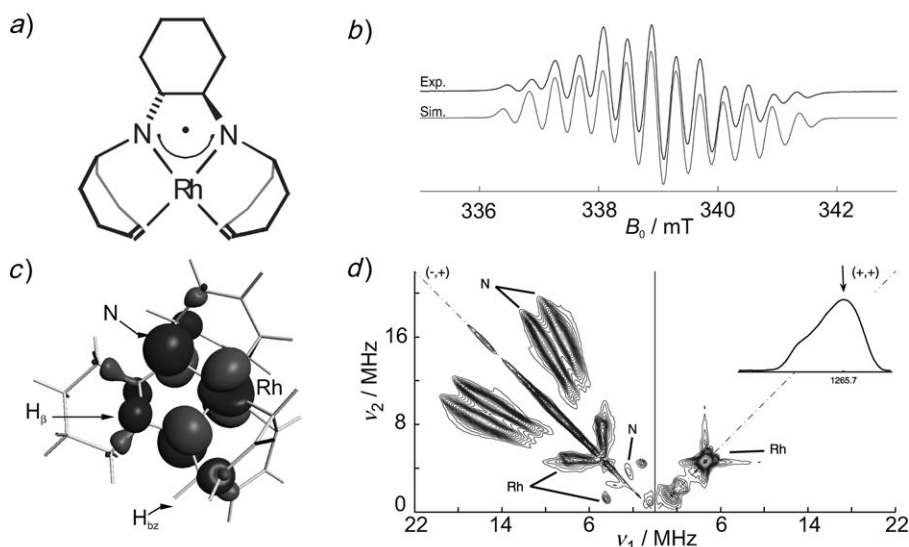
Fig. 16. a) *Sketch of [Rh(trop₂dach − 2H)]˙. b) X-Band CW-EPR spectrum measured at 298 K, experiment* (Exp.) *and simulation* (Sim.). c) *Plot of the SOMO for the model compound [Rh(cht₂dach)]˙* (cht = cycloheptatrienyl). d) *Matched Q-band HYSCORE spectrum measured at 25 K near to the g_2 observer position* (see inset, cross-peaks from ^{103}Rh and ^{14}N are labelled). Figures adapted from [■].

ple, [Rh(trop₂dach − 2H)]˙ reacts with Bu₃SnH, PhSH, and the silane Et₃SiH, whereas [Rh(trop₂N˙)(bipy)]⁺ reacts with Bu₃SnH, and PhSH but not with the silane Et₃SiH. This reactivity, which takes place at the N-center(s), further indicates that a significant part of the spin density is localized there, and that the tetracoordinated [Rh(trop₂-dach − 2H)]˙ complex is more reactive than the pentacoordinated aminyl-radical complex [Rh(trop₂N˙)(bipy)]⁺.

Transition-metal-coordinated aminyl radicals have long been searched for because of their close resemblance to phenoxy-radical metal complexes, [ML$_n$(OR˙)], a very important class of metalloenzymes [57]. This work demonstrates how such complexes can be synthesized and their electronic structure characterized in detail.

3.3. *Three-Spin Nitroxide–Copper–Nitroxide Clusters Coupled by a Strong Exchange Interaction.* An unusual exchange-coupled three-spin cluster has been observed in the (hexafluoroacetylacetonato)copper complex [Cu(hfac)₂] with two pyrazol-4-yl-substituted 'nitronyl-nitroxides' L^{Pr} (R = Pr) [58]. This complex belongs to a recently discovered family of heterospin polymer-chain complexes which have generated considerable interest in the field of molecular magnetism. The polymer chains consist of alternating coordination units CuO₄N₂ and CuO₆, which contain single-spin >N−Cu²⁺−N< and three-spin >N−˙O−Cu²⁺−O˙−N< clusters, respectively (*Fig. 17*).

The complexes with [Cu(hfac)₂L^{Pr}] undergo structural rearrangements at low temperatures with accompanying magnetic effects that were monitored with CW EPR. *Fig. 18,a* shows X-band CW-EPR spectra of the polycrystalline powder measured between 90 and 260 K. The spectra consist of the usual pattern from Cu²⁺ ions ($g_{||}$ = 2.08, $g_⊥$ = 2.37) superimposed on a broad line with $g ≈ 1.85 - 2.0$ which grows with lowering

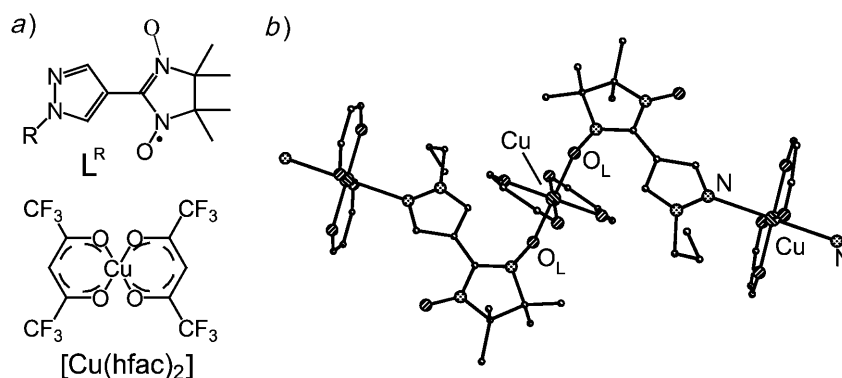Fig. 17. a) *Structures of [Cu(hfac)$_2$] and the nitroxide ligand L^R, and* b) *the polymer-chain structure of the [Cu(hfac)$_2$L^{Pr}] (R=Pr) complexes.* Adapted from [58].

temperature. The former spectrum was assigned to the single-spin unit >N−Cu^{2+}−N<, and the latter one to the three-spin cluster >N−$\cdot$O−Cu^{2+}−O$\cdot$−N< in the spin state $S=\frac{1}{2}$. Measurements at Q-band, shown in *Fig. 18,b*, yield the same g values for the '$g<2$ signals' determined at X-band, demonstrating that they are due to an electron *Zeeman* interaction. However, the '$g<2$ signals' cannot be explained by either the g values of the copper complex or the nitroxide radical ($g\approx2.0$).

The spin Hamiltonian for a three-spin system $\cdot$O−Cu^{2+}−O$\cdot$ can be written as $\mathscr{H}=g_1\beta\mathbf{B}_0(\hat{\mathbf{S}}_{1z}+\hat{\mathbf{S}}_{3z})+g_2\beta\mathbf{B}_0\hat{\mathbf{S}}_{2z}-2J(\hat{\mathbf{S}}_1+\hat{\mathbf{S}}_3)\hat{\mathbf{S}}_2$. Subscripts 1 and 3 correspond to the spins of the two nitroxide moieties, and subscript 2 corresponds to the spin of the Cu^{2+} ion. For simplicity, it was assumed that the g values for the Cu^{2+} ion and nitroxide moieties are isotropic, and that both nitroxide moieties are equivalent. The eigenstates of the Hamiltonian are a quartet $S=\frac{3}{2}$ state, and two doublet $S=\frac{1}{2}$ states. For $|J|\gg B_0$, five transitions with three different frequencies can be observed. The three equivalent transitions between quartet sublevels have effective $g=(2g_1+g_2)/3$, and the two doublets have $g=g_2$ and $g=(4g_1-g_2)/3$. The latter doublet has $g<2$, since $g_1\approx2$ and $g_2>2$, and it is the lowest in energy for $J<0$. Taking into account also the polarization effect, the observed spectra were explained as due to antiferromagnetic coupling within the three-spin cluster.

This example shows how the field-dependent interactions (electron *Zeeman*) can be distinguished from field-independent interactions (spin–spin) by using a multi-frequency EPR approach.

4. Conclusion. – This review has concentrated on demonstrating how ENDOR and ESEEM spectroscopy is used to study disordered systems. These two methods, along with field-swept EPR experiments, provide a means to obtain a detailed description of the EPR parameters of paramagnetic centers in single crystals, powders, and frozen solutions. To obtain the most accurate EPR parameters requires not one technique alone but a combination, and preferably applied at several m.w. frequencies.

For ESEEM experiments in particular, the B_0 field strength needs to be matched to the hyperfine interaction of interest; the largest echo envelope modulation occurs when
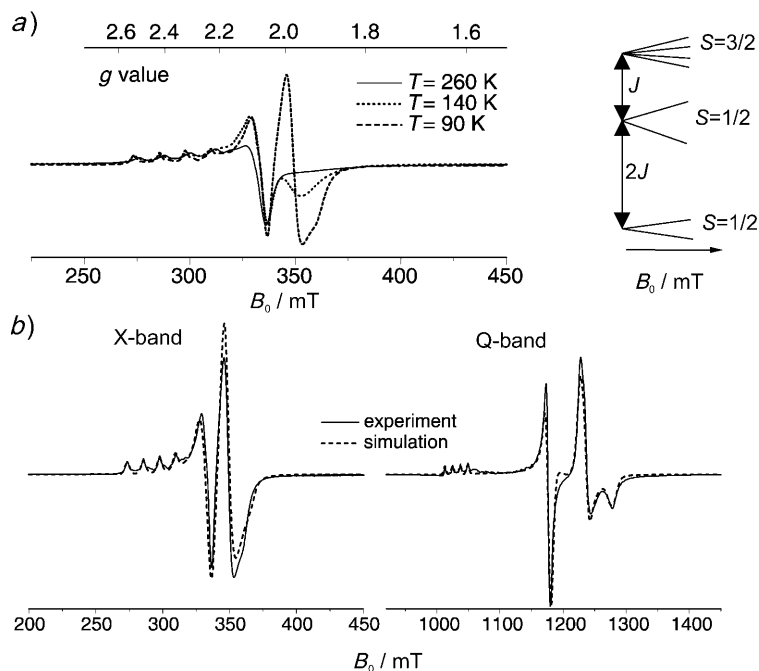
Fig. 18. a) *X-Band EPR spectra of [Cu(hfac)₂Lᴾʳ] measured at 9.72 GHz as a function of temperature.*
b) *Experimental and simulated X-band and Q-band* (34.17 GHz) *EPR spectra of [Cu(hfac)₂Lᴾʳ] at 90 K.* g Values used in the simulations: CuO_4N_2 unit, Cu^{II} $g_{\parallel}=2.371$, $g_{\perp}=2.075$; CuO_6 unit, L^{Pr} $g=2.007$, Cu^{II} $g_x=2.047$, $g_y=2.097$, $g_z=2.287$; $J=-115$ cm^{-1}. Inset: energy-level diagram. Figures adapted from [58].

the nuclear *Zeeman* and hyperfine interaction are equal in magnitude (strictly true only for $I=\frac{1}{2}$ nuclei). For a nucleus with a particular hyperfine interaction, the modulation depth may be too weak to observe at X-band, whereas at Q-band the sensitivity can be a maximum. Even when the modulation depth is predicted to be low for a particular nucleus, sensitivity improvements can conveniently be achieved by using matched pulses with an optimized m.w. field strength and length [59]. Examples are given in the application section.

Generally, ENDOR resolution is superior at higher B_0 fields. However, for nuclei with low γ_n values and large hyperfine couplings, the sensitivity may be better at lower fields (X-band) because the ENDOR enhancement effect allows very short π r.f. pulses to be used. Additionally, the EPR spectrum is less spread out (particularly from a transition metal) and thus, more orientations contribute to the measurement.

DEER Spectroscopy provides a straightforward method to measure the distance between two (or more) electrons by using two m.w. frequencies to excite 'observer' and 'pump' spins separately. Here, we have explained how the second m.w. pulse can be effectively replaced with a bichromatic pulse consisting of an m.w. and an r.f. pulse. This is advantageous when a second m.w. source is not available, or may even allow experiments that need many m.w. frequencies to be easily implemented. At pres-

ent, there is a three-frequency version of DEER that is applied to systems with three unpaired electrons.

Spectrum simulation is an integral part of EPR spectroscopy of disordered systems. To obtain the most accurate EPR parameters, it is usually necessary to measure (ENDOR or ESEEM) spectra at a number of observer positions across the EPR spectrum. Ideally, spectra at enough field positions should be recorded so that the set contains signals from all orientations of the paramagnetic center with respect to $\mathbf{B}_0$. The number required depends on the width of the EPR spectrum. In disordered systems, spectra measured away from the extreme edges of the field-swept EPR spectrum consist of ridges whose widths reflect the anisotropy of the spin Hamiltonian parameters, and the orientation selection. Sharp peaks are usually observed at 'single-crystal' positions, making their interpretation straightforward. Once the data have been collected, each field position needs to be correctly interpreted and the signals simulated. For time-domain experiments, usually a computer program based on the density matrix formalism [60] is implemented. Examples include EasySpin [22] and XSophe [61]. 1D Time-domain experiments, such as two-pulse or three-pulse ESEEM, can be simulated quickly with this approach. This allows in some situations a fitting algorithm to be implemented. However, simulation of 2D experiments such as HYSCORE are very time-consuming, particularly if more than one nuclear spin needs to be considered, for high-spin-number nuclei, and if $S > \frac{1}{2}$. In these cases, we suggest that a scan of possible solutions first be undertaken by computing just the frequency positions of the cross-peaks by exact diagonalization of the spin Hamiltonian. This calculation is very rapid, and the correct orientation selection can be included. Once possible solutions are found, they should be checked with a simulation which includes both position and intensity information. For ENDOR, very often simulation programs calculate the nuclear frequencies and transitions by diagonalization of the spin Hamiltonian, an approach appropriate for resonance irradiation. In this case, appropriate care should be taken when comparing this simulation to pulse ENDOR spectra (*e.g.*, blind spots, pulse selectivity, *etc.*).

Once the EPR parameters are determined, they need to be interpreted in terms of chemical structure. For example, hyperfine couplings give the spin populations in s- and p-type orbitals, and electron–nuclei distances. An emerging tool in this respect is the calculation of EPR parameters from the electronic structure calculated by DFT [62]. The accuracy obtained by using this method is often able to discriminate between different proposed chemical models. Usually, EPR parameters for the ligands are reliably calculated, but for the transition metal they need to be treated with care. The techniques presented in this review provide a means to obtain very detailed information from paramagnetic samples.

REFERENCES

[1] F. Gerson, W. Huber, 'Electron Spin Resonance Spectroscopy of Organic Radicals', Wiley-VCH, Weinheim 2003.
[2] J. D. Harvey, C. J. Ziegler, *Coord. Chem. Rev.* **2003**, *247*, 1; S. K. Pushpan, S. Venkatraman, V. G. Anand, J. Sankar, H. Rath, T. K. Chandrashekar, *Proc. Indian Acad. Sci., Chem. Sci.* **2002**, *114*, 311.
[3] A. Schweiger, G. Jeschke, 'Principles of Pulse Electron Paramagnetic Resonance', Oxford University Press, 2001.
[4] B. M. Hoffman, *Acc. Chem. Res.* **2003**, *36*, 522.
[5] B. M. Hoffman, *Proc. Natl. Acad. Sci. U.S.A.* **2003***, 100*, 3575.
[6] Y. Deligiannakis, M. Louloudi, N. Hadjiliadis, *Coord. Chem. Rev.* **2000***, 204*, 1.
[7] K. V. Lakshmi, G. W. Brudvig, *Curr. Opin. Struct. Biol.* **2001**, *11*, 523.
[8] T. Prisner, M. Rohrer, F. MacMillan, *Annu. Rev. Phys. Chem.* **2001***, 52*, 279.
[9] D. Goldfarb, D. Arieli, *Annu. Rev. Biophys. Biomol. Struct.* **2004**, *33*, 441.
[10] C. Gemperle, A. Schweiger, *Chem. Rev.* **1991**, *51*, 1481.
[11] L. G. Rowan, E. L. Hahn, W. B. Mims, *Phys. Rev. A* **1965**, *137*, 61.
[12] W. B. Mims, *Phys. Rev. B* **1972**, *5*, 2409.
[13] A. Ponti, A. Schweiger, *Appl. Magn. Reson.* **1994**, *7*, 363.
[14] G. Jeschke, A. Schweiger, *Mol. Phys.* **1996**, *88*, 355.
[15] A. Pöppl, L. Kevan, *J. Phys. Chem.* **1996**, *100*, 3387.
[16] E. R. Davies, *Phys. Lett. A* **1974**, *47*, 1.
[17] W. B. Mims, *Proc. R. Soc. London, Ser. A* **1965**, *283*, 452.
[18] A. D. Milov, K. M. Salikhov, M. D. Shirov, *Sov. Phys., Solid State* **1981**, *24*, 565.
[19] M. Fedin, M. Kälin, I. Gromov, A. Schweiger, *J. Chem. Phys.* **2004**, *120*, 1361.
[20] M. Kälin, I. Gromov, A. Schweiger, *Phys. Rev. A* **2004**, *69*, 033809.
[21] S. Stoll, A. Schweiger, *J. Magn. Reson.* **2006**, *178*, 42.
[22] S. Stoll, A. Schweiger, http://www.easyspin.ethz.ch.
[23] S. Stoll, A. Schweiger, *Chem. Phys. Lett.* **2003**, *380*, 464.
[24] S. Stoll, A. Schweiger, in 'Biological Magnetic Resonance', Eds. J. Berliner and M. Hemminga, Vol. 27, Kluwer Academic/Plenum Publishers, New York, in press.
[25] S. A. Dikanov, A. M. Tyryshkin, M. K. Bowman, *J. Magn. Reson.* **2000**, *144*, 228.
[26] S. Stoll, C. Calle, G. Mitrikas, A. Schweiger, *J. Magn. Reson.* **2005**, *177*, 93.
[27] S. Stoll, A. Schweiger, *J. Magn. Reson.* **2003**, 163, 248.
[28] P. J. Chmielewski, L. Latos-Grażyński, K. Rachlewicz, T. Glowiak, *Angew. Chem., Int. Ed.* **1994**, *33*, 779.
[29] H. Furuta, T. Asano, T. Ogawa, *J. Am. Chem. Soc.* **1994**, *116*, 767.
[30] A. Ghosh, *Angew. Chem., Int. Ed.* **2004**, *43*, 1918.
[31] J. L. Sessler, D. Seidel, *Angew. Chem., Int. Ed.* **2003**, *42*, 5134.
[32] P. J. Chmielewski, L. Latos-Grażyński, *Coord. Chem. Rev.* **2005**, *249*, 2510.
[33] G. R. Geier, D. M. Haynes, J. S. Lindsey, *Org. Lett.* **1999**, *1*, 1455.
[34] H. Furuta, N. Kubo, H. Maeda, T. Ishizuka, A. Osuka, H. Nanami, T. Ogawa, *Inorg. Chem.* **2000**, *39*, 5424.
[35] J. D. Harvey, C. J. Ziegler, J. Telser, A. Ozarowski, J. Krzystek, *Inorg. Chem.* **2005**, *44*, 4451.
[36] P. J. Chmielewski, L. Latos-Grażyński, I. Schmidt, *Inorg. Chem.* **2000**, *39*, 5475.
[37] G. Mitrikas, C. Calle, A. Schweiger, *Angew. Chem., Int. Ed.* **2005**, *44*, 3301.
[38] U. Ermler, W. Grabarse, S. Shima, M. Goubeaud, R. K. Thauer, *Science (Washington, D.C.)* **1997**, *278*, 1457.
[39] R. K. Thauer, *Microbiology* **1998**, *144*, 2377.
[40] M. Goubeaud, G. Schreiner, R. K. Thauer, *Eur. J. Biochem.* **1997**, *243*, 110.

[41] J. Harmer, C. Finazzo, R. Piskorski, C. Bauer, B. Jaun, E. C. Duin, M. Goenrich, R. K. Thauer, S. Van Doorslaer, A. Schweiger, *J. Am. Chem. Soc.* **2005**, *127*, 17744.

[42] C. Finazzo, J. Harmer, C. Bauer, B. Jaun, E. C. Duin, F. Mahlert, M. Goenrich, R. K. Thauer, S. Van Doorslaer, A. Schweiger, *J. Am. Chem. Soc.* **2003**, *125*, 4988.

[43] C. Finazzo, J. Harmer, B. Jaun, E. C. Duin, F. Mahlert, R. K. Thauer, S. Van Doorslaer, A. Schweiger, *J. Biol. Inorg. Chem.* **2003**, *8*, 586.

[44] D. Hinderberger, R. P. Piskorski, M. Goenrich, R. K. Thauer, A. Schweiger, J. Harmer, B. Jaun, *Angew. Chem.* **2006**, *118*, 3684; *Angew. Chem., Int. Ed.* **2006**, *45*, 3602.

[45] B. Jaun, *Helv. Chim. Acta* **1990**, *73*, 2209; W. Grabarse, F. Mahlert, E. C. Duin, M. Goubeaud, S. Shima, R. K. Thauer, V. Lamzin, U. Ermler, *J. Mol. Biol.* **2001**, *309*, 315; M. Goenrich, E. C. Duin, F. Mahlert, R. K. Thauer, *J. Biol. Inorg. Chem.* **2005**, *10*, 333; E. C. Duin, L. Signor, R. Piskorski, F. Mahlert, M. D. Clay, M. Goenrich, R. K. Thauer, B. Jaun, M. K. Johnson, *J. Biol. Inorg. Chem.* **2004**, *9*, 563.

[46] a) V. Pelmenschikov, M. R. A. Blomberg, P. E. M. Siegbahn, R. H. Crabtree, *J. Am. Chem. Soc.* **2002**, *124*, 4039; b) V. Pelmenschikov, P. E. M. Siegbahn, *J. Biol. Inorg. Chem.* **2003**, *8*, 653; c) K. P. Jensen, U. Ryde, *J. Phys. Chem. A* **2003**, *107*, 7539.

[47] J. S. Griffith, *Nature (London)* **1957**, *180*, 30.

[48] I. García-Rubio, J. I. Martínez, R. Picorel, I. Yruela, P. J. Alonso, *J. Am. Chem. Soc.* **2003**, *125*, 15846.

[49] G. Merényi, J. Lind, in 'N-Centered Radicals', Ed. Z. Alsfassi, Wiley, New York, 1998, p. 599–613; B. J. Maxwell, J. Tsanaktsidis, in 'N-Centered Radicals', Ed. Z. Alsfassi, Wiley, New York, 1998, p. 663–684.

[50] J. Stubbe, W. A. van der Donk, *Chem. Rev.* **1998**, *98*, 705.

[51] Y. Miura, T. Tomimura, *Chem. Commun.* **2001**, 627; Y. Miura, T. Tomimura, Y. Teki, *J. Org. Chem.* **2000**, *65*, 7889.

[52] a) M. J. Ingleson, M. Pink, J. C. Huffman, H. Fan, K. G. Caulton, *Organometallics* **2006**, *25*, 1112; b) W. Kaim, R. Gross, *Angew. Chem., Int. Ed.* **1985**, *24*, 856.

[53] a) F. N. Penkert, T Weyhermüller, E. Bill, P. Hildebrandt, S. Lecomte, K. Wieghardt, *J. Am. Chem. Soc.* **2000**, *122*, 9663; b) E. Kogut, H. L. Wiencko, L. Zhang, D. E. Cordeau, T. H. Warren, *J. Am. Chem. Soc.* **2005**, *127*, 11248.

[54] T. Büttner, J. Geier, G. Frison, J. Harmer, C. Calle, A. Schweiger, H. Schönberg, H. Grützmacher, *Science (Washington, D.C.)* **2005**, *307*, 235.

[55] P. Maire, M. Königsmann, A. Sreekanth, J. Harmer, A. Schweiger, H. Grützmacher, *J. Am. Chem. Soc.* **2006**, *128*, 6578.

[56] K. Ray, T. Weyhermüller, A. Goossens, M. W. J. Crajé, K. Wieghardt, *Inorg. Chem.* **2003**, *42*, 4082; E. K. Beloglazkina, A. A. Moiseeva, A. A. Chizhevskii, B. N. Tarasevich, N. V. Zyk, K. P. Butin, *Russ. Chem. Bull., Int.Ed.* **2003**, *52*, 1990; ref. [1] in F. Breher, C. Böhler, G. Frison, J. Harmer, L. Liesum, A. Schweiger, H. Grützmacher, *Chem.–Eur. J.* **2003**, *9*, 3859.

[57] P. Chaudhuri, K. Wieghardt, *Prog. Inorg. Chem.* **2001**, *50*, 151; W. Kaim, *Dalton Trans.* **2003**, 761.

[58] M. V. Fedin, S. L. Veber, I. A. Gromov, V. I. Ovcharenko, R. Z. Sagdeev, A. Schweiger, E. G. Bagryanskaya, *J. Phys. Chem. A* **2006**, *110*, 2315.

[59] G. Jeschke, A. Schweiger, *Mol. Phys.* **1996**, *88*, 355.

[60] K. Blum, 'Density Matrix Theory and Applications', Plenum, New York, 1981.

[61] D. Wang, G. R. Hanson, *Appl. Magn. Reson.* **1996**, *11*, 401; G. R. Hanson, K. E. Gates, C. J. Noble, M. Griffin, A. Mitchell, S. Benson, *J. Inorg. Biochem.* **2004**, *98*, 903.

[62] F. Neese, E. I. Solomon, in 'Magnetism: Molecules to Materials IV', Ed. J. S. Miller and M. Drillon, Wiley-VCH, Weinheim, 2002.